

Hydrogen boron fusion in confined geometries

Marco Tosca^{1,2}, Dimitri Batani³, Lorenzo Giuffrida¹, Philippe Nicolai³, Clement Caizergues³, Daniele Margarone¹, Didier Raffestin³, Evgeny Filippov⁴, SA Pikuz⁴, Katarzyna Liliana Batani⁵, Qiran Cai⁶, Srikanth Mateti⁶, Ying Chen⁶, Kohei Yamanoi⁷, Alessio Morace⁷

¹ELI Beamlines Facility, The Extreme Light Infrastructure ERIC, Dolní Brežany, Czech Republic.

²Charles University, Faculty of Mathematics and Physics, Department of Macromolecular Physics, Prague, Czech Republic.

³University of Bordeaux, CELIA, Domain du Haut Carré, 43 Rue Pierre Noailles, 3405 Talence, France

⁴HB11 Energy Holdings Pty, Freshwater 2096, Australia

⁵Institute of Plasma Physics and Laser Microfusion (IPPLM), Warsaw, Poland

⁶Institute for Frontier Materials, Deakin University, Waurn Ponds, Victoria 3216, Australia

⁷Institute of Laser Engineering, Osaka University, 2-6 Yamada-oka, Suita 565-0871, Japan

Abstract

High-energy, short-pulse laser-driven proton–boron (p–B) fusion has attracted growing interest due to its aneutronic character and potential for clean energy generation. In this study, we report on two experimental campaigns carried out at the LFEX laser facility using petawatt-class laser systems (energy ~ 1.2 – 1.4 kJ, pulse duration 2.7 ps, peak intensity ~ 2 – 3×10^{19} W/cm²). The experiments explored the influence of complex target geometries—including spherical, cylindrical, and wedge-shaped configurations—on α -particle yield. Our results demonstrate that spherical targets can enhance α -particle production by up to two orders of magnitude compared to planar targets of identical composition and also lead to a noticeable shift of the α -particle energy spectrum toward higher values.

Furthermore, we implemented a novel diagnostic technique for unambiguous α -particle detection using a CR-39 detector integrated into a Thomson parabola spectrometer. Particle-in-cell (PIC) simulations performed with the Smilei code provide additional insight into the role of self-generated magnetic fields in modulating particle dynamics. These simulations highlight the critical interplay between target geometry, confinement effects, and fusion efficiency. Overall, our findings underscore the potential of optimized target designs to significantly enhance fusion yield and α -particle output in p–B fusion, with promising implications for the development of laser-driven α -particle sources and advanced clean energy concepts.

Key words

Hydrogen boron fusion; α -particles; Thomson parabola; CR-39; boron nitride; high-intensity lasers; laser-induced nuclear reactions

1. Introduction

Laser-driven proton–boron (p–¹¹B) fusion has become a topic of significant interest due to its aneutronic nature and potential applications in clean energy production. The reaction $p + {}^{11}\text{B} \rightarrow 3\alpha + 8.7 \text{ MeV}$ [1] is particularly appealing, as it results solely in the emission of α -particles. Numerous experiments have reported α -particle yields [2, 3, 4, 5, 6, 7, 8], with some kilojoule-class laser systems achieving yields in excess of 10^{10} – 10^{11} α -

This peer-reviewed article has been accepted for publication but not yet copyedited or typeset, and so may be subject to change during the production process. The article is considered published and may be cited using its DOI.

This is an Open Access article, distributed under the terms of the Creative Commons Attribution licence (<https://creativecommons.org/licenses/by/4.0/>), which permits unrestricted re-use, distribution, and reproduction in any medium, provided the original work is properly cited.

10.1017/hpl.2025.10055

particles per laser shot [⁹,¹⁰]. These results underscore the increasing capabilities of modern high-power laser facilities to initiate and sustain such nuclear reactions.

However, despite these promising developments, the observed α -particle production in most of these experiments is primarily attributed to "beam fusion"—a process in which the reaction rate scales linearly with the number of laser-accelerated protons directly interacting with boron nuclei. This mechanism lacks evidence for secondary processes or fusion cascades that could substantially amplify the yield. As a result, the achievable α -particle output remains constrained by initial beam parameters, target geometry, and the laser energy delivered to the interaction region.

In this context, exploring confined geometries—such as focusing the laser into a closed boron-containing target—offers a potentially transformative approach to enhance α -particle generation. Unlike flat targets, confining targets allow accelerated protons and boron ions to undergo multiple interactions with the target material, effectively extending their interaction path and time, thereby increasing the likelihood of fusion events.

Additionally, confined geometries can support the generation of strong self-induced electric and magnetic fields, driven by the intense laser–plasma interaction. In principle, these fields might further accelerate and confine the ions within the target volume, significantly enhancing the probability of fusion reactions. We performed particle-in-cell (PIC) simulations, which predict substantial field generation and complex particle dynamics in such geometries. A detailed discussion of these simulation results is presented in the final section of this paper.

In this context, we conducted an experiment at the LFEX laser facility at the Institute of Laser Engineering (ILE), Osaka University. LFEX is a high-energy, short-pulse laser system capable of delivering approximately 1.5 kJ within a 1 ps pulse, focused onto a ~ 50 μm diameter spot. The experiment aimed to investigate the influence of target geometry on fusion yield by comparing several target configurations, including flat foils, cylinders, spheres, and wedges. All targets were irradiated directly by the laser pulse—an arrangement commonly referred to as "in-target" or "direct irradiation" in laser-driven proton–boron fusion experiments.

The diagnostic setup included solid-state nuclear track detectors (CR-39) and a Thomson Parabola (TP) spectrometer positioned along the laser axis on the rear side of the targets. The TP spectrometer was used to measure the energy and species of generated ions, while α -particles were detected using CR-39 detectors. A novel method was developed in this study to unambiguously identify α -particles and distinguish them from other ion species. This technique involves placing CR-39 detectors inside the TP spectrometer, in combination with specifically selected filters. The method is detailed in Section 4.2 of this paper.

Complementing the experimental work, numerical simulations were performed for the spherical target configuration using advanced particle-in-cell (PIC) codes, which incorporate nuclear reaction models to accurately capture fusion processes.

2. Targets

In the experiment, we systematically compared various target geometries to assess their impact on α -particle generation and fusion efficiency. The geometries studied included cylindrical, spherical, and wedge-shaped targets. To isolate the effect of geometry, these were benchmarked against flat foil targets fabricated using the same procedure and materials as the spherical targets.

Additionally, boron nitride (BN) cylinders were compared to flat BN foil targets of 0.2 mm thickness, commercially sourced from Goodfellow and previously investigated in [⁹,¹⁰]. Wedge-shaped targets, also produced from the same BN foils used for the spheres, were included to explore the effects of partial confinement.

This section details the characteristics and fabrication methods of the targets, with particular emphasis on the closed-geometry configurations—namely, spheres and cylinders.

2.1. Preparation of boron nitride spheres

Boron nitride spheres were produced at the ILE target preparation laboratory (see Fig. 1). The boron-containing capsule and film targets were fabricated by dispersing B_2O_3 nanopowder into a polystyrene matrix. The B_2O_3 powder (model 1520DX, 99.5% purity, average particle size: 80 nm) was sourced from SkySpring Nanomaterials. To improve uniformity of dispersion, the nanopowder surface was treated with silane coupling agents prior to mixing.

The modified B_2O_3 powders and polystyrene were mixed in 1,2-dichloroethane solution with 0.9 wt% [11]. The mixture was then spread onto a glass substrate and the solvent was allowed to evaporate, forming thin films. Capsule targets were fabricated via an emulsion method using a polyvinyl alcohol (PVA) solution [12, 13, 14]. The resulting capsules had a diameter of approximately 500 μm and a wall thickness of 18 μm , with an entrance hole of 200 μm in diameter.

The boron concentration was estimated at ~ 10 wt% in both the film and capsule structures. However, despite the silane treatment, as seen in Fig. 1, the B_2O_3 nanoparticles were not uniformly distributed within the polystyrene matrix, potentially contributing to fluctuations in the experimental results.

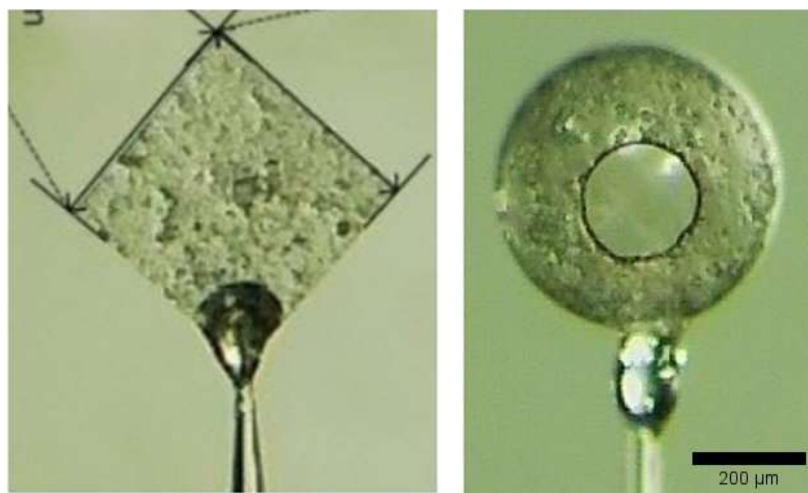


Fig. 1: Left) flat foil target (1mm \times 1mm); Right) sphere target (500 μm diameter)

Flat foils of doped-CH, also shown in Fig. 1, were produced using the same procedure and were used for comparison.

2.2. Wedge targets

For comparison, in addition to simple doped CH foils, we also used “wedge” targets, as shown in Fig. 2. The goal of these targets was to have a semi-confined geometry (partially confined and only in 1 direction) in order to distinguish the effects due to the confinement and the presence of a second wall.

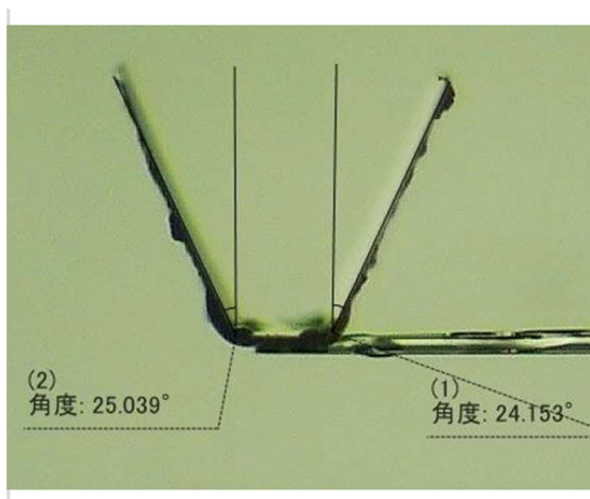


Fig. 2: Example of wedge targets produced with the same technique as flat foils and sphere targets

2.3. Preparation of boron nitride cylinders

Boron nitride cylinders were prepared starting from boron nitride nanosheets which were synthesized by mechanochemical process using hexagonal (h-) BN powders as starting materials. h-BN (Momentive grade, 99% purity) were purchased from Momentive Performance Materials Inc. Boron nitride nanosheets with -NH₂ functional groups were synthesized as in [15].

The X-ray diffraction patterns of the BN nanosheets (Fig. 3a) comprises all the prominent diffraction peaks of the h-BN with a reduced peak intensity. The broadened peak shape indicates reduced thickness and size of h-BN basal planes [16]. Sample morphology was examined using Scanning Electron Microscopy (SEM) with a Hitachi S4500 Zeiss Supra 55VP instrument operated at 3 kV. A SEM image of produced BN nanosheets is shown in Fig. 3b, which shows the size range of the BN nanosheets of an average diameter of 1 μm and thickness of 10 nm [17].

Selected area electron diffraction and high-resolution imaging of nanosheets were performed using Transmission Electron Microscopy (TEM), a JEOL JEM 2100F instrument with an acceleration voltage of 200 kV and equipped with a Gatan Quantum ER 965 Imaging Filter. The transmission electron microscopy (TEM) image in Fig. 3c shows the resulting BN nanosheets has a highly crystalline structure.

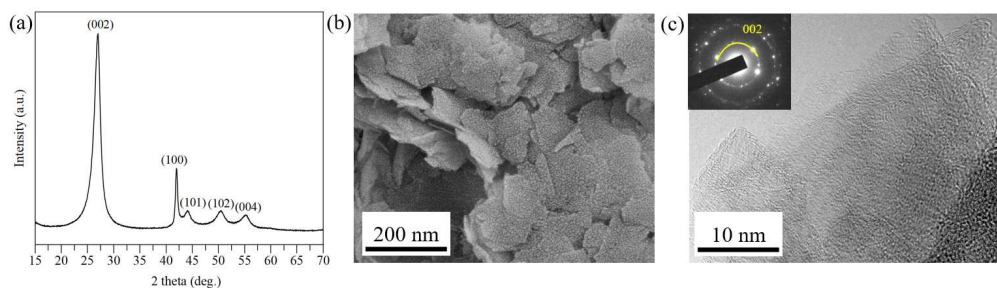


Fig. 3: XRD pattern (a), SEM images (b), HR-TEM image (c) of boron nitride nanosheet target.

The cylindrical BN was produced using a template method with a commercially available optical fiber, zeonex, with a 500 μm diameter. Initially, a 250 nm layer of polymethyl methacrylate (PMMA) was dip-coated onto the zeonex surface, employing a PMMA/anisole solution. Subsequently, a 10-20 μm thick layer of BN nanosheets was dip-coated onto the zeonex/PMMA fibers, utilizing a 46 mg/mL BN nanosheets dispersion in ethanol [18]. To enhance the mechanical strength of the thin BN coatings, a ~1 μm layer of polyvinyl alcohol (PVA) coating was applied. The removal of the zeonex/PMMA template was achieved by immersing it in cyclohexane at approximately 75 °C for a duration of 3 hours. The various phases of the preparation procedure are shown in Fig. 4.

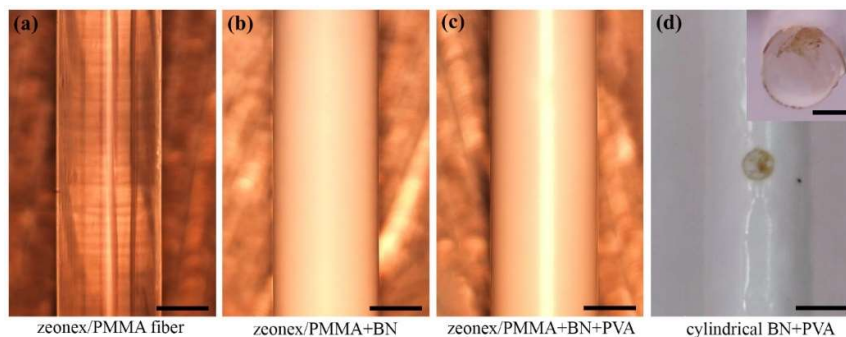


Fig. 4: (a-c) Optical images illustrating a zeonex fiber with various coatings, and (d) a digital photograph of the cylindrical BN after the removal of the zeonex template. The insert displays the cross-section of the cylindrical BN. Scale bar: 250 μm .

Due to differences in chemical composition between the cylindrical targets and the spherical and wedge targets, a direct comparison of their performance against reference shots using simple boron-doped CH foils was not feasible. To address this limitation and provide a consistent basis for evaluating the cylindrical targets, we selected 200 μm -thick boron nitride (BN) foils—commercially available from Goodfellow—as the appropriate reference material.

3. Experimental set-up

3.1 Laser

The experiment was carried out at the Institute of Laser Engineering of the University of Osaka in Japan using the short-pulse, high intensity, high energy PW class laser LFEX [19]. Two experimental campaigns were made, in February and July 2022 for a total of 21 laser shots. Laser energies varied between 1.2 and 1.4 kJ, in 2.7 ± 0.45 ps at the fundamental wavelength ($\lambda=1.05$ μm). The focal spot diameter on target was ~ 50 μm , full width at half maximum, corresponding to a laser intensity of $2\text{-}3 \times 10^{19}$ W/cm^2 . The scheme of the experimental set-up is shown in Fig. 5.

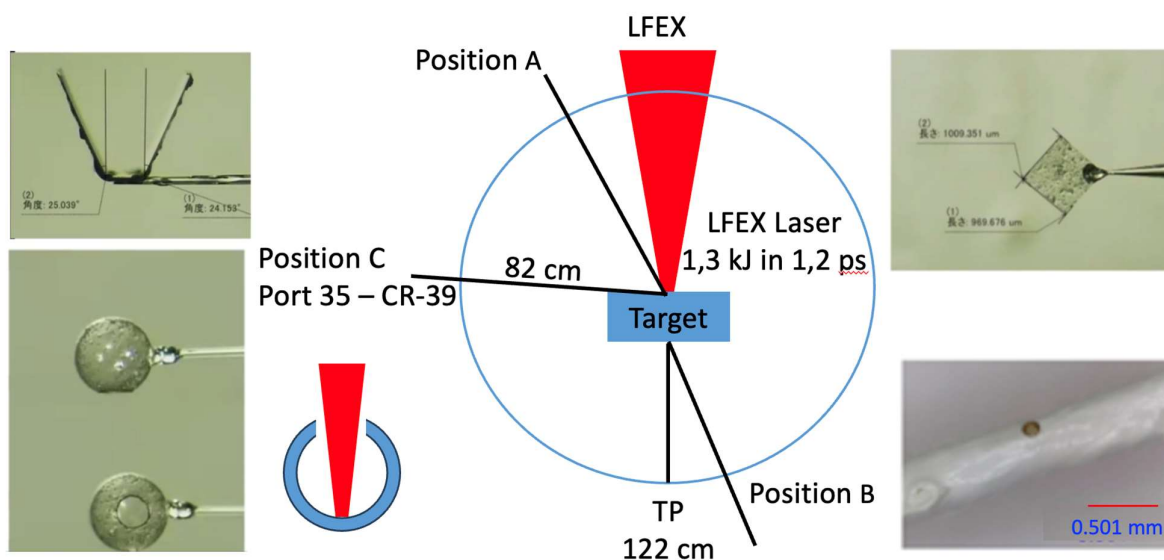


Fig. 5: Arrangement of the experimental set-up showing positions (A, B, C) where CR-39 foils were placed and the relative distances. Also shown the position and distance of the Thomson Parabola Spectrometer and, again, the various types of targets used in the experiment. Position A corresponds to 10° from the front target normal, B to 10° from the rear target normal, C to 80° from the front target normal

3.2 CR-39 detectors

CR-39 detectors, previously calibrated to distinguish α -particles and protons, were in 3 different positions (see Fig. 5). In particular, the analysis is mainly focused on the CR-39 placed in position C were placed at an angle of 80° from the target. Indeed, as shown for instance in ref [20], protons and heavy ions produced by the TNSA (target normal sheath acceleration) mechanism [21, 22, 23, 24] are mainly emitted perpendicularly to the target within a narrow cone. Therefore, at an angle of 80° the detector is less contaminated by ions and hence this strategic positioning provides the highest and cleanest signal from α -particles. CR-39 detector placed in position A and B were also intended for α -particle detection, at these angles however, due to heavy ions contamination, the detector became saturated early in the etching process, making it very hard to distinguish the α -particles.

After the irradiation CR-39 detectors were etched in a 6.25M NaOH solution for 1 hour, employing the methods detailed in [25]. To enhance energy detection and prevent detector saturation from low-energy particles, aluminum (Al) filters were placed before the CR-39. The thicknesses were of 20, 50 and 70 μm for the February campaign and of 10, 20 and 40 μm for the July campaign. Our calibration of CR-39 allowed to identify α -particles with energy between 0.96 and 4.8 MeV. However, when a filter is inserted, the energy loss must be taken into account, allowing the investigation of energies above the one set during the calibration. The energy range of a α -particles detected when 20 μm Al filter is insert is 5.27 to 7.67 MeV, while for the 50 μm Al filter it is 9.17 to 10.95 MeV.

3.3 Thomson parabola

The Thomson parabola (TP) was used for the measurement of ion yield and energy distribution in the experiment. The typical image is demonstrated in Fig. 6 wherein different tracks correspond to different ratios of Q/M , where Q is the ion charge and M is the ion mass. The applied electric and magnetic fields were 3.5×10^5 V/cm, and 0.75 T. The TP was installed normally to the back side of the laser-irradiated target. The diagnostic solid angle was 8.3×10^{-9} . Spectra were registered on fluorescence detectors Image Plates (IP, TR type). Ion sensitivity of IP was simulated by SRIM [26] according to ref.s [27, 28]. Ion tracks were processed using a python code. The low-energy cutoff for protons was about 3 MeV for the mentioned values of electric and magnetic field. The maximum proton energy measured in the experiment was about 40 MeV in the case of $E_{\text{las}}=1.3$ kJ on the target. Due to the low solid angle of the observation and the same Q/M ratio for He^{2+} and C^{6+} ions, it is not possible to record α -particles, at least when IP is used as a detector.

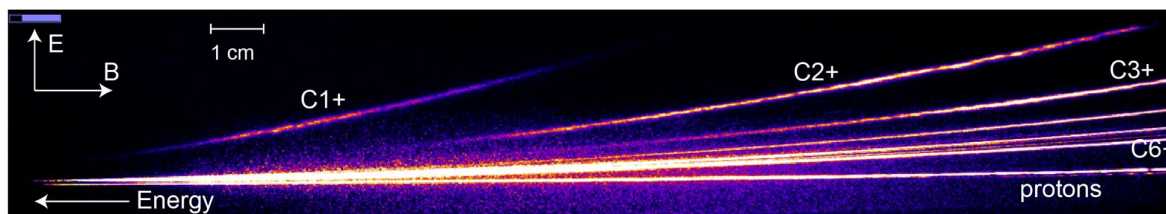


Fig. 6: Example of typical TP image in the experiment. The image is registered on the TR-type Image Plate and shows energetic distribution of different ion species of Carbon and Hydrogen.

4. Experimental Results

Table 1 summarizes the shots performed on LFEX in two campaigns

| Shot N. | Campaign | Energy, kJ | Target | CR-39 | TP |
|---------|---------------|------------|---------|-------|----|
| 1 | February 2022 | 1.189 | CH foil | √ | √ |
| 2 | February 2022 | 1.238 | Sphere | √ | √ |

| | | | | | |
|----|---------------|-------|----------------------|---|-------|
| 3 | February 2022 | 1.236 | Wedge | ✓ | ✓ |
| 4 | February 2022 | 0.606 | Sphere | ✓ | ✓ |
| 5 | February 2022 | 1.193 | Sphere | ✓ | ✓ |
| 6 | February 2022 | 0.752 | Flat | ✓ | CR-39 |
| 7 | February 2022 | 1.296 | Sphere | ✓ | ✓ |
| 8 | February 2022 | 1.205 | Wedge | ✓ | ✓ |
| 9 | February 2022 | 1.180 | Flat | ✓ | ✓ |
| 10 | February 2022 | 1.205 | Wedge | ✓ | ✓ |
| 11 | February 2022 | 0.655 | Sphere | ✓ | ✓ |
| 12 | February 2022 | 1.173 | Sphere | ✓ | ✓ |
| 1 | July 2022 | 1.300 | CH | ✓ | ✓ |
| 2 | July 2022 | 1.350 | Sphere | ✓ | ✓ |
| 3 | July 2022 | 1.260 | Flat | ✓ | ✓ |
| 4 | July 2022 | 1.301 | Sphere | ✓ | ✓ |
| 5 | July 2022 | 1.350 | Cylinder | ✓ | ✓ |
| 6 | July 2022 | 0.876 | Cylinder | ✓ | ✓ |
| 7 | July 2022 | 1.254 | BN 200 μm | X | X |
| 8 | July 2022 | 1.277 | Flat | ✓ | ✓ |
| 9 | July 2022 | 0.710 | Sphere | ✓ | CR-39 |

Tab. 1: Summary of performed shots with indications of working diagnostics (✓). Total 21 shots of which 9 on spheres, 3 on wedges, and 4 on flat foils. Imaging Plates (IP) were used as detectors in the TP apart from two shots where this was replaced by a CR-39 foil.

4.1 Measurements of proton and ion emission

The Thomson Parabola (TP) spectrometer was used to measure proton emission from the laser-irradiated targets and to identify and differentiate ions of various species, particularly carbon ions. In addition, the TP enabled the measurement of ion energy spectra and yields throughout the experiment. Determining the proton yield is crucial, as it directly influences the evaluation of the efficiency of the proton–boron (pB) fusion reaction. The measured proton yields for different target configurations are presented in Fig. 7a, while the corresponding results for carbon ions are shown in Fig. 7b. Notably, the highest proton yield was observed for the flat targets, including the undoped CH reference target.

It should be noted that TP data were only collected during the July 2022 experimental campaign, as the spectrometer was not employed during the February session.

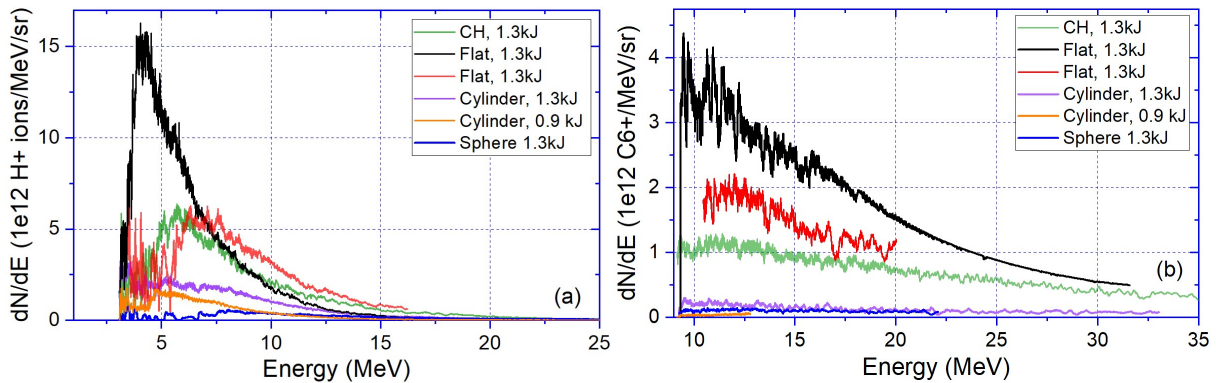


Fig. 7: Thomson parabola results for (a) protons and (b) C^{6+} ions. The spectral range was limited by the edge of the detector and the merging point of all tracks (for C^{6+} ions) where it is not possible to distinguish different ion species.

The data for C^{1+} ions, presented in Fig. 8, exhibit a similar trend: flat foils are the most efficient in generating carbon ions, whereas spherical and cylindrical targets yield significantly fewer ions.

It is important to note that the lower proton and carbon ion yields observed for spherical and cylindrical targets, as compared to flat foils, may be partially attributed to geometrical effects. In the Target Normal Sheath Acceleration (TNSA) mechanism, ions are typically emitted perpendicularly to the target surface. For

curved geometries such as spheres and cylinders, this can result in a broader angular distribution of emitted particles. Additionally, even minor misalignments may cause ions to be emitted in directions that deviate from the TP spectrometer axis, leading to reduced detection efficiency.

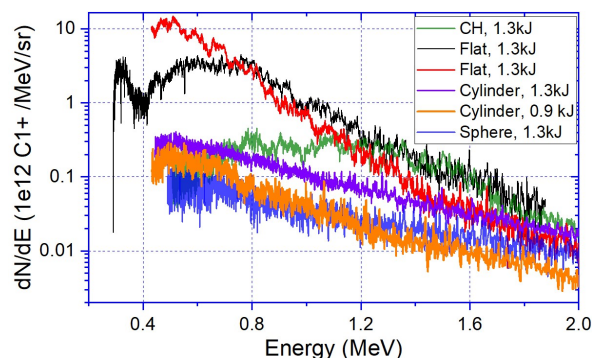


Fig. 8: Thomson parabola results for C1+ ions.

4.2 Measurement of α -particles

The investigation of α -particles is of paramount importance in this study. CR-39 was the main diagnostic to measure α -particle yield. In addition, in order to improve α -particles detection, a new approach was implemented, i.e. we performed a dedicated shot on a sphere target with laser energy of 700 J (Shot 9) and, instead of imaging plates, the TP employed a large CR-39 covered with a $11 \pm 1 \mu\text{m}$ Al filter.

Fig. 9a displays the scanned raw traces obtained after 1 hour of etching of the CR-39. It is possible to see one line corresponding to the $Q/M = 0.5$. This trace includes all ions like $^{12}\text{C}^{6+}$, $^{10}\text{B}^{5+}$ and α -particles. The yellow circled region is critical: the $Q/M = 0.5$ line is appearing, meaning that ions are acquiring sufficient energy to pass through the $11 \pm 1 \mu\text{m}$ Al filter. In this region, the main contribution is given by α -particles and C^{6+} ion both having the same energy per nucleon (1 MeV/u). Notably, in the first small segment of the line, α -particles with 4 MeV can reach the detector with a remaining energy of 1.4 MeV, while 12 MeV C^{6+} ions are stopped by the filter. The inset of Fig. 9a zooms in the region in which α -particles and carbon ions are both coexisting.

Fig. 9b illustrates the area distribution of low-energy ions that passed through the filter in the yellow-circled region. The analysis advanced from left to right, capturing a sequence of 30 images in a row, corresponding to a total length of 11.7 mm. However, as the process continued, the prevalence of energetic carbon ions became prominent, making difficult the distinction with α -particles. The area distribution is showing two peaks which were fitted with 2 Gaussian functions: the first peak in black matched the area of α -particles with energies between 1-1.4 MeV after the filter, as shown in the calibration used in [25], and 3.7-4 MeV before the filter. The second peak in red is attributed to the contribution of C^{6+} or $^{10}\text{B}^{5+}$ ions. The convolution of the two peaks (green line) is matching the experimental data (red line).

The potential presence of D^+ ions, which share the same $Q/M = 0.5$ as α -particles, should also be taken in consideration. An approach similar to the one we are demonstrating in this article has been used for the distinction of D^+ and C^{6+} ions in laser-driven ion acceleration [29]. However, based on our etching calibration and the known behavior of proton tracks, D^+ ions are not expected to contribute significantly under our etching conditions. Moreover, deuterium is not intentionally introduced into the targets and would only appear as a minor contaminant. Therefore, we consider the D^+ contribution to be negligible in our analysis.

The analysis of the TP revealed that α -particles with energies ranging from 3.7 to 4 MeV occupied the same position. The observed presence of a carbon signal is likely attributable to an inconsistency in the thickness of the Al foil: a $10 \mu\text{m}$ Al foil permits the detection of 12 MeV carbon ions, while a $11 \mu\text{m}$ foil does not. The α -particles measured using this method was extrapolated from the result of the fit which includes the possible carbon overlap. A total of 228 tracks, were measured, amounting to 3.35×10^9 α -particles /sr. Additionally, the low laser energy of this shot prevented the saturation of CR-39 covered with $10 \mu\text{m}$ Al filter

in position A, B and C (while the rest of shots at higher laser energies were generally saturated). The resulting yield of α -particles in position C was $1.59 \times 10^9 \pm 11\%$ /sr, which is consistent with the one of the TP (taking into account the different angles of the TP and the CR-39).

This notable result demonstrates, for the first time to our knowledge, the possibility to discriminate the α -particles from C^{6+} ions in a TP. However, this technique remains time-consuming and offers limited energy discrimination, with considerable uncertainties arising from the intrinsic energy resolution of CR-39, variations in etching conditions, and the cumulative propagation of errors across the multiple measurement steps required for the analysis. These limitations highlight the need for further research to enhance the accuracy, efficiency, and energy resolution of CR-39-based diagnostic methods.

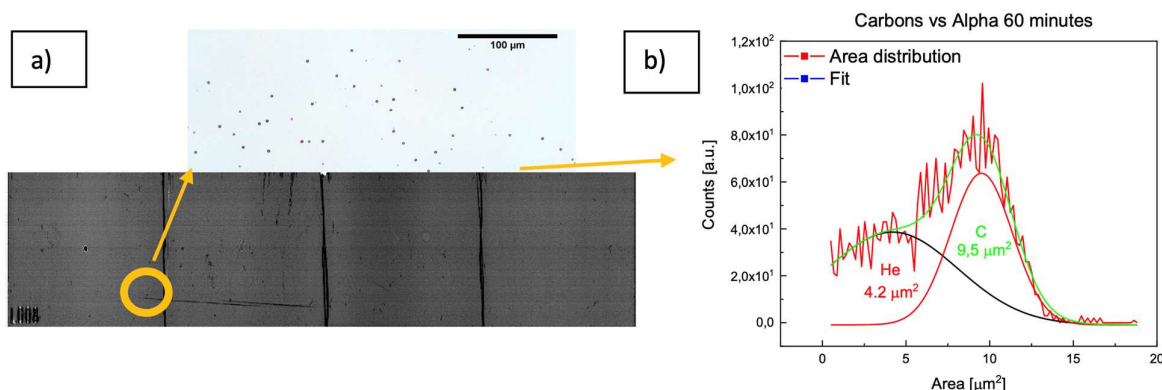


Fig.9: a) raw traces of CR-39 covered with 11 μm Al filter used as IP on the TP. In yellow the region of the trace $q/m=0.5$ used to detect α -particles. Magnified region of the circle is placed as an inset. b) Area distribution showing two different ion species. The one peaked at 4.2 μm^2 is identified as α -particles while the second peak at 9.5 μm^2 is identified as carbon ions.

Concerning the results obtained from CR-39 foils, the analysis is somewhat complicated due to the fact that in the two campaigns we used different sets of filters (10, 20 and 40 μm in July, 20, 50 and 70 μm in February) but also to the shot-to-shot fluctuations in the laser pulse, and to the non-uniform boron concentration in the targets (as noticed in section 2.1) which could sometimes produce fluctuations up to a factor of 10 in α -particle yield from shot to shot.

Fig. 10 compares α -particle emissions from various target types measured on the CR-39 in position C. In this graph, the results obtained with 40 μm and 50 μm filters have been plotted with the same color, in order to get a clearer idea of the general trends. The arrows indicate that the corresponding CR-39 was saturated. While in this case α -particle yield cannot be computed, it certainly implies that more ions and more α -particles are produced. Let's notice that in similar shots with flat targets, the CR-39 was never saturated. The comparison of the results for sphere targets and flat targets shows that α -particle yield increases by a factor ~ 3 for 10 and 20 μm filters, by a factor ~ 10 for the 40 and 50 μm filters, and by a factor ~ 100 for 70 μm filters. This shows that for sphere targets there are many more α -particles but also that their spectrum is likely shifting to higher energies (The cut-off energies for α -particles and ions in Al filters are shown in table 2).

Such increments are probably underestimated because, in the case of sphere targets, it is not possible to estimate the α -particle yield for saturated shots. Indeed, these values have been obtained by considering a few shots in which CR-39 were not saturated with the corresponding filters. In general, CR-39 with a 10 μm Al filter and laser energy of ≈ 1.3 kJ were saturated because of an insufficient distance of the detector from TCC. Shot 9 in July 2022 with 0.71 kJ was instead exploitable and provided results which are fully compatible with those obtained with the TP.

All reported shots are well above the background level which was measured on a non-irradiated CR-39 and corresponds to 2×10^6 /sr.

| Ion | Cutoff energy [MeV] | | | | |
|---------------------------------------|---------------------|-------|-------|-------|-------|
| | 10 | 20 | 40 | 50 | 70 |
| Al filter thickness [μm] | | | | | |
| H | 0.77 | 1.24 | 1.94 | 2.23 | 2.74 |
| He | 2.75 | 4.71 | 7.60 | 8.79 | 10.89 |
| C | 11.65 | 22.19 | 38.29 | 44.99 | 56.80 |

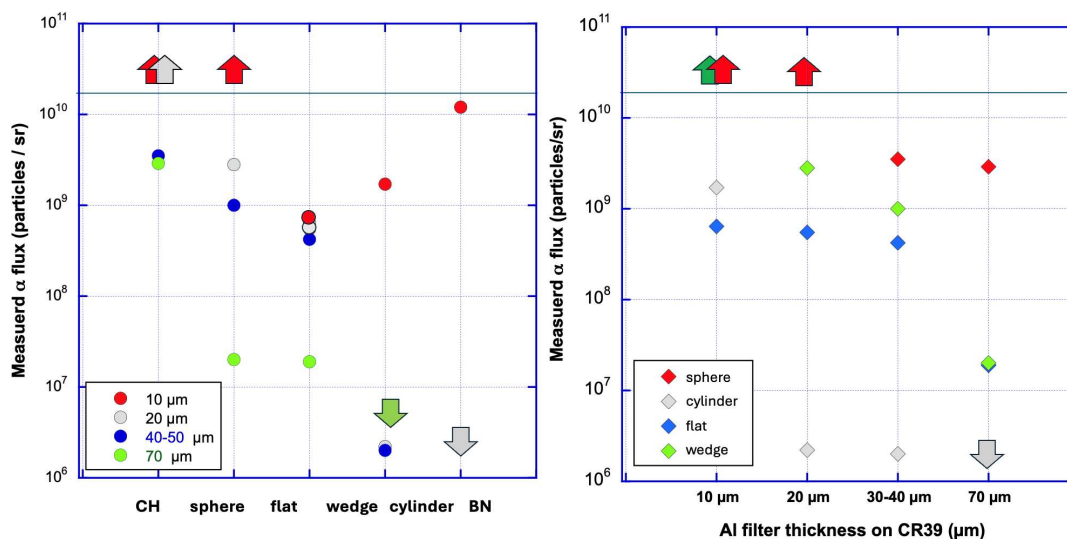
Tab 2: Cut-off energy vs. Al filter thickness for protons, α -particles and carbon ions

Fig.10: Measured α -particle flux extracted from CR39 placed in position C (80° from the target) vs. target type (left) and Al filter thickness in μm (right). The up-arrows indicate that in that case the signal on CR-39 was saturated, corresponding to a higher ion flux. The down-arrows correspond to signals equal or below background level measured on a non-irradiated CR-39 ($\sim 2 \times 10^6$ /sr). Each filter thickness corresponds to an energy range for detected α -particles: 10 μm Al \rightarrow 3.46–5.45 MeV; 20 μm Al \rightarrow 5.26–6.89 MeV; 40 μm Al \rightarrow 8.01–9.29 MeV; and 70 μm Al \rightarrow 11.22–12.23 MeV (notice that the lower energies for each filter do not coincide with the cut-off energy from table 2 because the values here take into account the calibration of CR-39 for α -particles).

For sake of clarity, error bars have been added only in the left graph. Notice that for the case of spheres, error bars are smaller due to the larger number of shots.

Despite the limited number of shots performed with wedge (3) targets, the results appear to be intermediate between those obtained with spherical and flat targets. Indeed, the core of our results is the quantitative comparison between spheres, wedges, and flat foils. All such targets were made with the same procedure and included boron oxide as a dopant.

As cylinders could not be realized using the same procedure, and were based on boron nitride, a direct comparison with spheres and wedge targets is not possible. The chemical composition of the cylindrical targets (pure BN with plastic coatings) differs from the plastic-based targets doped with boron oxide (B_2O_3) nano powder, potentially affecting the fusion yield. For comparison, Fig. 10 shows also the commercially available 200 μm thick flat BN foils produced 1.2×10^{10} α -particles/sr with a 10 μm filter [9]. These results are therefore just added for qualitative comparison

The α -particle yield from cylinder targets remained below $\sim 10^9$ α -particles/sr for the 20 μm filter, with only marginally detectable traces for the 50 μm filter, barely above the CR-39 background. This unexpectedly low performance is challenging to interpret (as discussed further in the simulation section) and is likely influenced by shot-to-shot fluctuations and limited statistics.

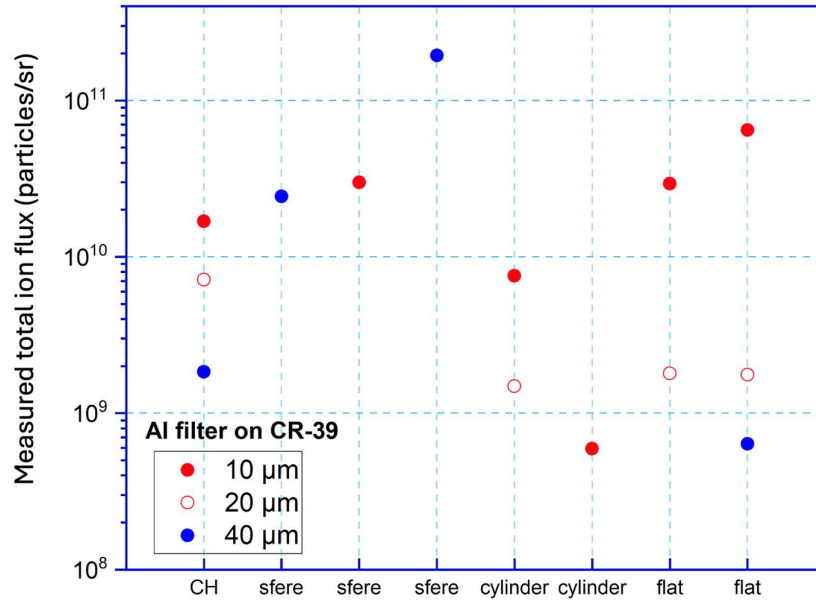


Fig.11: Total ion flux (summing all species detected on CR39) measured in position B for the 8 LFEX shots performed in the July 2022 experimental campaign

Finally, in Fig. 11 are shown the results obtained from the CR-39 in position B during the July experiment. Here the CR-39 is placed at 178.5 cm far from TCC on target rear side at almost perpendicular to target surface (we cannot simply compare with the results in February 2022 because the CR-39 was put at a different distance, 132cm, and at an angle $\sim 45^\circ$).

As mentioned before, in this position the CR-39 can be polluted due to other ions impinging on the foil. For instance, it is well known that energetic carbon ions (35-60 MeV) produce tracks on CR-39 which are very similar to those from α -particles (see Fig. 3 of ref. [30]). However, the behavior is similar to what reported in Fig. 10 with the best results obtained from spheres (up to 2×10^{11} ions /sr for a 40 μm Al filter).

5. Simulations

The particle-in-cell (PIC) code Smilei [31] has been used to simulate in 2D geometry the laser plasma interaction. Two target geometries have been tested, the planar and the spherical ones. In 2D, the spherical and cylinder targets correspond to the same simulation due to the missing third dimension. For this reason, the results we present are primarily intended to provide a qualitative comparison and contribute to understanding the underlying physical phenomena.

In the simulations, the laser pulse profile was Gaussian in space and time with 2×10^{19} W/cm² peak intensity, 1054 nm central wavelength, 1.5 ps duration, and 60 μm spot, which corresponds to the 1.3 kJ on target recorded on average in the experiments. Target wall thicknesses were 20 μm , for the sphere the cavity radius and entrance hole diameters are 500 μm and 200 μm , respectively, in agreement with the experimental specifications. The simulation domain was $1000 \times 1000 \mu\text{m}^2$ for the planar case and $1250 \times 1000 \mu\text{m}^2$ for the sphere, with 30 nm mesh size. To compare the results of 2D simulations with experimental results, we assumed a 3D transverse extension leading to the correct laser pulse energy.

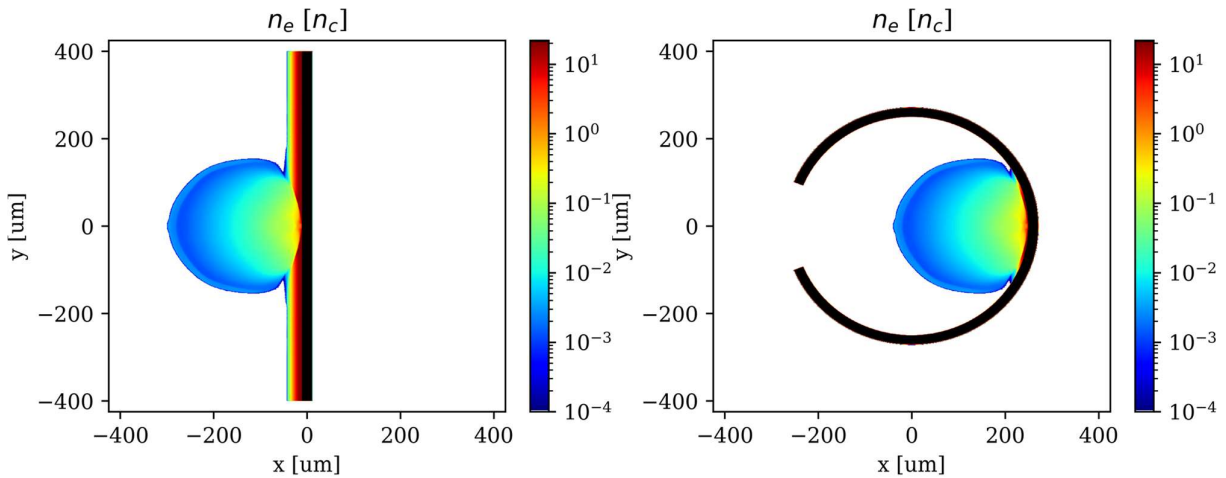


Fig. 12: Initial electron density in the planar and the spherical geometries.

In the experiment, due to Amplified Spontaneous Emission (ASE) induced in the laser system, a large pre-plasma was already present in front of the focal region when the main laser pulse arrived on target. The initial pre-plasma profile was simulated with the hydrodynamics code TROLL [32] for the planar target. The same pre-plasma was then used also for the spherical case, limiting the plasma extension to the cavity interior. The maximum density was set to 20 times the critical density n_c . To limit the number of species in the simulations, we consider a pure BH target. To reduce further the numerical cost of simulations, targets were pre-ionized (B^{3+} , H^+) and no collision was modeled. The two deepest Boron levels involve typical ten times higher ionization energies than other levels and are not expected within the core target prior to the main pulse arrival. As for collisions, they would affect accelerated ions propagation by slowing down the ions and limiting the traveled distances, with the likely effect of decreasing the fusion yield with respect to what obtained from collisionless PIC simulations.

Each simulation cell with matter initially contains 20 macro-electrons and 8 macro-ions per ion species, that is a number of macro-particles approaching one hundred, except in the plasma region where the number of macro particles was doubled. The electronic densities at simulation start are reported in Fig. 12. The dense part corresponding to the solid shell is highlighted in black. In the planar case, a density profile is present also outside the focal spot region due to the limitations in the equation of state used in the hydrodynamic code. This artificial contribution will be distinguished from the solid part in evaluating the fusion reactions, as explained later on. In the sphere case, this plasma expansion is geometrically cropped by the shell walls.

To evaluate the number of created α -particles, we post-processed PIC results using a Monte-Carlo analysis. At each output time, a constant fraction of the macro-particles was extracted from the simulation. The proton and boron ions were randomly paired provided they were in the same cell of a coarse Cartesian grid, with approximately 3 μm mesh size. The fusion reaction rate was then computed over the associated pairs as:

$$\sum_{(1,2)} \sigma(E_{1,2}) w_1 w_2 V_{1,2}$$

where $E_{1,2}$ is the energy in the center of mass and $V_{1,2}$ the relative velocity, with w_1 and w_2 the associated weights of respectively particle 1 and particle 2. The nuclear cross-section σ corresponded to the fusion process between p and ^{11}B leading to a 3- α event, with a maximum of 1200 mb near 600 keV in the center of mass. This reaction appears as the dominant α source for energies below 4 MeV. Such energy range is relevant for the direct irradiation scheme, which accelerates particles to lower energies as compared to the TNSA process. As nuclear reactions are not handled directly in the PIC simulations, this method only allows evaluating fusion events while p and ^{11}B are not depleted following the fusion reaction events and α -particles are not transported in the target.

To retrieve the experimental conditions, we must compensate for the reduced target density used in the simulations. Considering a true solid density with full ionization of about 300 n_c leads to a factor 10 on ions

in the solid shell. However, this over-ponderation should not be applied to pre-plasma nor to the accelerated particles which otherwise would overestimate the kinetic energy transmitted by the laser. In practice, we only over-weight particle pairs having at least one particle with energy below 100 keV and initially belonging to the solid shell, i.e. one accelerated particle crossing a dense cold part. This approximation is especially justified by the drop of the fusion cross-section for energies below 150 keV. In the planar case, the expansion density ramp in front of surface, outside the focal spot region, will be accounted as a plasma component in the fusion yield calculation, that is without the over-weighting correction.

The total 3α yields for the sphere and planar cases are shown in Fig. 13a. The reference time corresponds to the arrival of the laser intensity maximum on target. For both cases, we note a first intense peak starting with the pulse onset and lasting for approximately 5 ps, i.e. far after the termination of the laser pulse. Indeed, protons have first to travel from the pre-plasma to the shell, then continue to trigger nuclear reactions during their travel time through the thickness of the solid-state shell, thus the typical time of flight of 600 keV protons over 20 μm is 2 ps. Accordingly, the output frequency for PIC post-processing was set to every 200 fs, i.e. much smaller than the laser duration and travel time of ions of most interest. Indeed, as visible from Fig. 13a the fusion rate evolution curves present smooth aspects which advocates for a good numerical resolution of fusion processes in space and time. In the sphere case, the confined geometry is characterized by further fusion events with two later peaks. The integrated number of fusion reactions (Fig. 13b) highlights the dominant contribution of these additional events in comparison to the first peak summed yield, increasing the total event number by a factor of ~ 5 in comparison to the planar case.

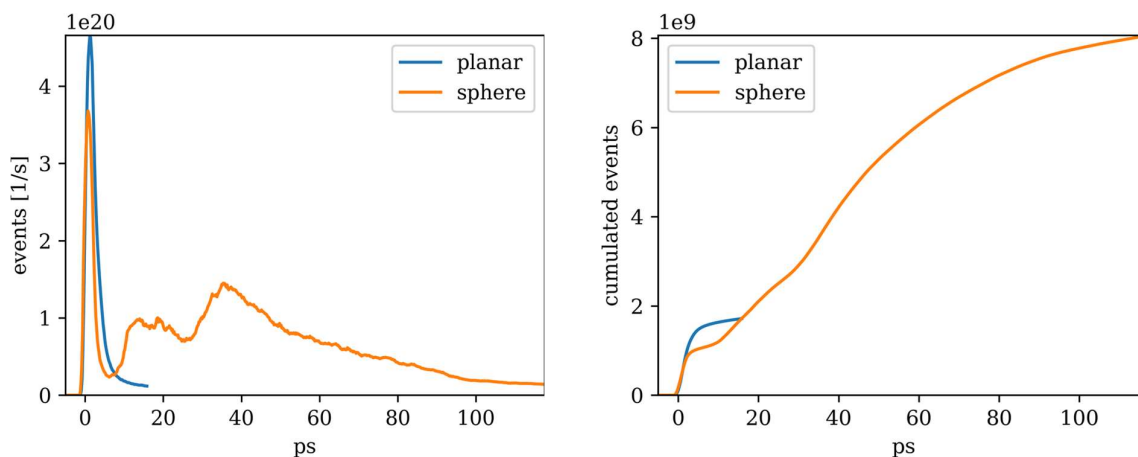


Fig. 13: Evaluation of p-B11 fusion events in planar vs. spherical geometry. (left) Time evolution of fusion rate (right) Time integrated yield. For the spherical case we see three characteristic phases corresponding to the first emission peak, an intermediate bump, the final peak.

Fig. 14 shows the spatial location of the fusion events for the planar and sphere cases in different time intervals. Here, Fig.s 14a and 14b correspond to the first peak time for the two geometries. We can see that reactions occur essentially in the vicinity of the laser spot, in the solid shell backing the pre-plasma. This observation is consistent with fusion driven by ions accelerated from the front plasma and pushed forward inside the target, coherently with the hole-boring mechanism [33]. Although laser energy is initially deposited in the pre-plasma area, this region does not appear as producing a large number of fusion reactions. In contrast to the hole boring phase, the fusion reactions arising at later times in the sphere case appear to involve the entire target, as shown in Fig. 14c.

Indeed, the low densities involved in the plasma plume hinder the fusion yields obtained from the short initial phase of non-linear laser-plasma interaction. This confirms that the direct calculation of fusion processes within the PIC simulation turns unnecessary here to get already a good evaluation of the number of fusion events and thus supports the validity of our lighter post-processing approach.

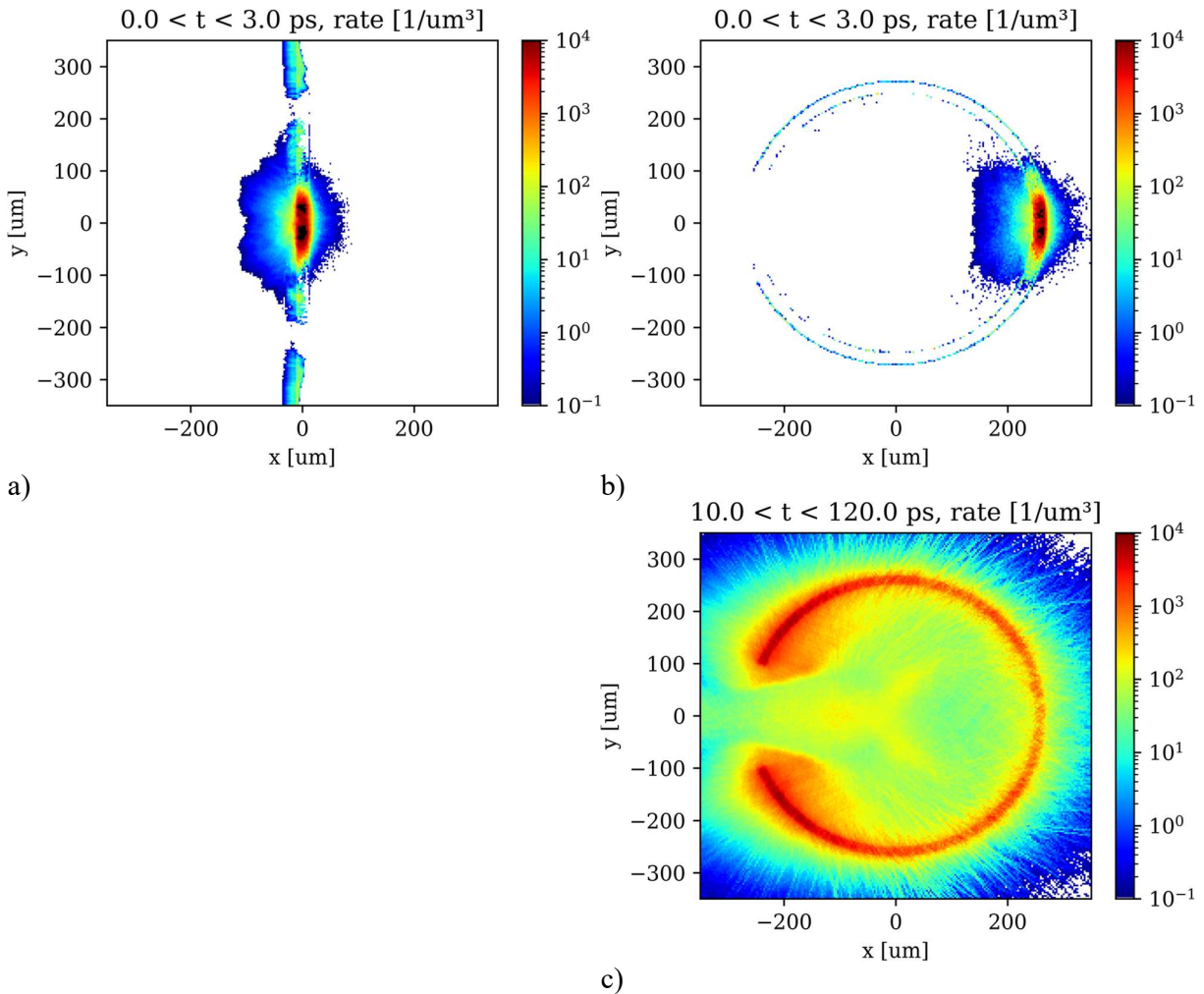


Fig. 14: Spatial location of fusion events (a) for planar geometry (b,c) for spherical geometry. Here (a,b) refer to the time of the first emission peak, (c) refers to emission at later times.

Fig. 15 shows the spatial distribution of average energy of boron ions, distinguishing the ions stemming from the pre-plasma (a) and those initially within the inner part of the solid shell (b) just after the first event peak. As ions are not relativistic, the natural dispersion in velocity translates into a drift in space leading to locally limited energy spreads. A population of low energy ions appears at the rear of the spherical shell ($x > 270 \mu\text{m}$). These have crossed the solid shell forward and correspond to the active region of Fig. 14b leading to the primary peak. However reported boron energies are generally below 6 MeV, which do not provide a high fusion probability. Hence, accelerated protons are the main responsible for the initial fusion events.

In Fig. 15b, boron ions appear to be accelerated normally to the shell internal surface as expected from the TNSA mechanism, following the dispersion of the hot electron cloud created by the laser-plasma interaction in the vicinity of the spot region. At the front of the pre-plasma, similar acceleration is produced in the backward direction, and, in addition, there is also a contribution from Coulomb explosion (see Fig. 15a).

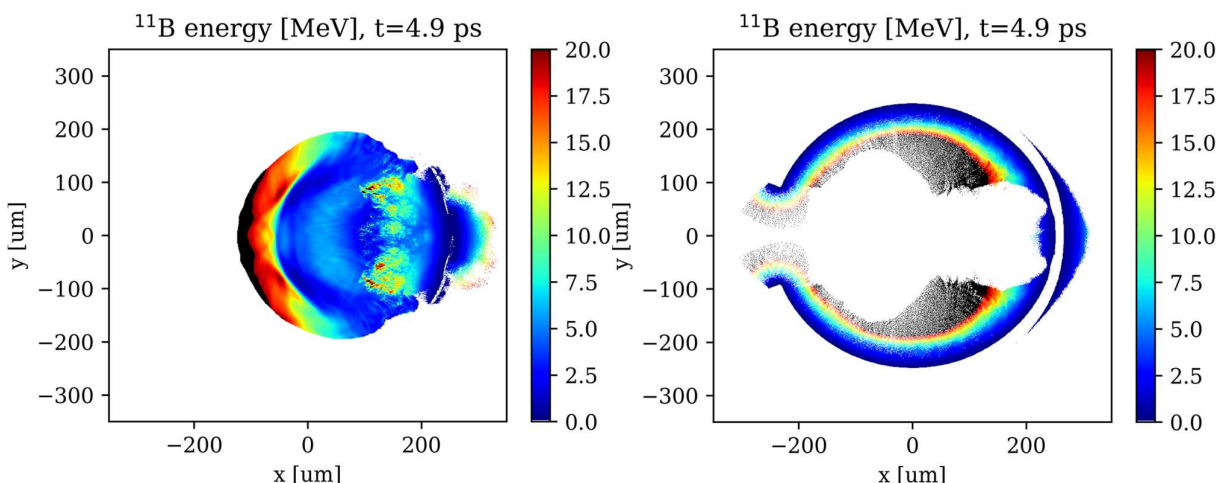


Fig. 15: Local average energy of boron ions originating (left) from the pre-plasma, and (right) from the internal part of the solid shell.

Altogether, ions are accelerated at higher energies than during the hole-boring phase and in more various directions, which explains the whole target activity observed in Fig. 14c. Fusion events then occurs along the proton and boron paths and presents a shape following the proton/boron current density. The long travel time across the sphere diameter explains the later activity in the sphere case. Moreover, the higher ion energies enable a higher kinetic energy transfer to α -particles, therefore resulting in more energetic α -particles.

These points are in good agreement with the experimental observations of α -particles with higher energies in confined geometries and of more α in the transverse direction, although TNSA emission of Carbon ions can also contribute to the observed CR-39 saturation for the sphere and the wedge targets.

We finally investigated the impact of self-generated magnetic field on fusion yield. As recalled in the introduction, the confined geometry can in principle bring to the generation of strong longer-lasting magnetic fields, as compared to the planar geometry, and these could act to confine the accelerated particles (electrons, protons, boron ions) thereby increasing the probability of reactions.

Unfortunately, the straight aspect of fusion path lines on Fig. 14c advocates against a fusion increase related to a confinement of ions by magnetic fields. However, magnetic fields could help to bending the ion trajectories making them intercept the solid shell, rather than escaping by the entrance hole, or increasing the crossing path length through the dense shell walls. Fig. 16 shows the magnetic field map obtained at two different times.

Large fields of typical ~ 2 kTesla intensity appear inside the cavity and last over tens of ps. For 600 keV protons the corresponding Larmor radius is ~ 56 μm . Instead for 6 MeV boron ions the Larmor radius exceeds the dimensions of the sphere. Hence only protons at energies relevant for the p- ^{11}B fusion may eventually be confined. Yet these fields are only present in the low-density plasma in the interior of the sphere, regions for which the fusion probability is weak due to low density. Also, no such intense magnetic fields are present at the shell exterior. This means that once a proton has crossed the sphere solid wall there is no field which can pull the proton backward, resulting in a single pass only. Hence, magnetic fields do not seem to contribute significantly to the increase of yield observed in spheres as compared to plane foils.

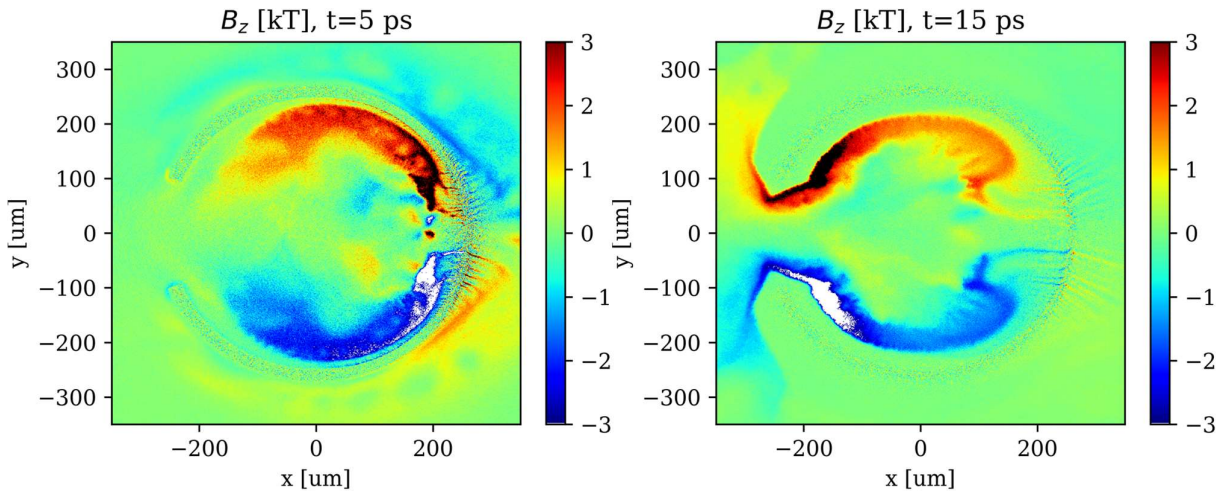


Fig. 16: Magnetic fields in the sphere case at two different times

A quantitative comparison between simulation and experiments would need further considerations as including the exact target composition and element distribution over the surfaces. Ideally, the emission of α -particles should be modeled within the PIC simulation to handle angular probabilities and align on detectors specific positions. At this stage, the obtained yields from the simulations appear lower than the ones deduced from the two experimental campaigns. While this statement can appear in contradiction with what we said about neglecting collisions in PIC simulations, we must bear in mind that many other effects are at play here, including the exact shape of the preplasma or of the laser pulse.

From Fig. 13b, one can conclude that the number of α -particles obtained from the PIC simulations rises to $6 \cdot 10^9$ and $2.4 \cdot 10^{10}$ respectively for the planar and spherical cases. However, all α -particles may not have enough energy to escape, and in particular one of the three produced α -particles has low energy. The best quantitative agreement seems to be obtained between the 2D PIC spherical case, i.e. akin to a cylinder, and the experimental cylinder targets with typical values of $2 \cdot 10^9 \alpha/\text{sr}$.

6. Conclusions

In this experiment, we investigated the influence of target geometry on α -particle yield. While variations in laser performance, target composition, and fabrication quality introduce uncertainties, statistically significant conclusions can be drawn by comparing spherical and flat foil targets, for which a sufficient number of shots were recorded. In this comparison, spherical targets consistently produced higher α -particle fluxes than flat foils. Specifically, the measured α -particle yield from spherical targets exceeded that of flat foils by a factor of ≥ 3 for 10 and 20 μm filters, ≥ 10 for 40 and 50 μm filters, and approximately 100 for 70 μm filters. These results not only indicate a greater number of α -particles generated with spherical targets but also suggest a shift in the α -particle energy spectrum toward higher energies.

This spectral shift may be attributed to differences in the dominant proton acceleration mechanisms for each geometry. In planar targets, fusion reactions are primarily driven by protons accelerated via the hole-boring mechanism. In contrast, spherical targets enable an additional population of protons to be accelerated by the Target Normal Sheath Acceleration (TNSA) mechanism from the inner surface of the cavity. These protons can then induce nuclear reactions on the opposite inner wall of the sphere. Since TNSA-accelerated protons generally possess higher energies than those produced by hole-boring, this could result in a higher energy transfer to the reaction products, leading to more energetic α -particles in the case of spherical targets.

In conclusion, α -particle production shows an increasing trend with plasma confinement (i.e. the spherical geometry seems to be better than wedge targets which are better than flat targets). This trend is supported by simulations which link TNSA emission (from simulations) to higher experimental α energies. Also, simulations suggest that the magnetic confinement effects are secondary in determining the increase in α -particles yield. This plausible conclusion conflicts with our initial expectations which partly motivated the experiment. Indeed B-fields of the order of ~ 1 kT imply a Larmor radius of the order of ~ 100 μm for 600 keV protons which is comparable to the target dimensions, thereby producing an insufficient confinement. In addition, magnetic fields are intense only in a limited area of the target and not in the high-density (solid) part of the target where α -particle production is maximized. However, in the future it will be interesting to investigate under which conditions (probably using smaller size spheres) it will be possible to increase the effect of the magnetic field and assess if there is a positive effect of magnetic field on α -particle yield.

Our results seem very encouraging, opening the path to further experiments. Unfortunately, high-energy high-intensity laser facility like LFEX only allow for a very low repetition rate (for LFEX this is ~ 3 shots/day). It is clear that the limited number of available shots, the variations in laser energy, diagnostic uncertainties, and the visible target non-uniformity, affect the reproducibility of the reported α -yield enhancements. In addition, many CR-39 foils were saturated making data interpretation more difficult. These results should therefore be interpreted as indicative rather than definitive, and future campaigns with improved target fabrication and additional laser shots will be necessary to refine and confirm the observed trends.

Another important point is indeed related to the use of CR-39 foils. In our experiment in many shots CR-39 foils were saturated (while sometimes those with thicker Al filters did not show signal above background noise level). Clearly this introduced a selection bias, as only unsaturated shots could be analyzed. Indeed, as explained in the paper, saturation can lead to underestimate real α -particle yields.

Finally, another important result of this experiment concerns the test of a method for unambiguously detecting α -particles against other ions (sec. 4.2 of the paper). This is based on using CR-39 foil detectors inside a Thomson Parabola spectrometer together with a set of Al filters of appropriate thickness allowing, in each position of the TP detector, to stop heavy ions while allowing α -particles to go through.

Acknowledgements

This work has been carried out within the framework of the EUROfusion Consortium, funded by the European Union via the Euratom Research and Training Programme (Grant Agreement No 101052200 — EUROfusion). Views and opinions expressed are however those of the author(s) only and do not necessarily reflect those of the European Union or the European Commission. Neither the European Union nor the European Commission can be held responsible for them. The involved teams have operated within the framework of the Enabling Research Project: ENR-IFE.01.CEA "Advancing shock ignition for direct-drive inertial fusion".

Co-authors from Deakin University gratefully thank the financial support from the Australian Research Council under the Linkage [LP200301537].

This work has also been supported by COST (European Cooperation in Science and Technology) through Action CA21128 PROBONO (PROton BORon Nuclear Fusion: from energy production to medical applicatiOns). MT and LG acknowledge the support of the Czech Science Foundation through Grant No. GACR24-11398S.

Finally, we acknowledge the support of HB11 Energy, Ltd, Australia, through its Collaborative Science Program.

References

- ¹ M. Oliphant and E. Rutherford, Proc. R. Soc. London A 141, 259 (1933).
- ² A. Picciotto, D. Margarone, A. Velyhan, P. Bellutti, J. Krasa, A. Szydlowsky, G. Bertuccio, Y. Shi, A. Mangione, J. Prokupek, A. Malinowska, E. Krousky, J. Ullschmied, L. Laska, M. Kucharik, and G. Korn, Phys. Rev. X 4, 031030 (2014)

- 3 I.C.E. Turcu, et al. "Borane ($BmHn$), Hydrogen rich, Proton Boron fusion fuel materials for high yield laser-driven Alpha sources" *Journal of Instrumentation*, 19, C03065 (2024) DOI: 10.1088/1748-0221/19/03/C03065
- 4 C. Labaune, C. Baccou, S. Depierreux, C. Goyon, G. Loisel, V. Yahia, and J. Rafelski, *Nat. Commun.* 4, 2506 (2013)
- 5 V. S. Belyaev, V. P. Krainov, A. P. Matafonov, and B. V. Zagreev, *Laser Phys. Lett.* 12, 096001 (2015).
- 6 Mark Aladi, et al. "Alpha particle yield in femtosecond laser-driven proton–boron fusion" *Eur. Phys. J. Spec. Top.* (2025) doi: 10.1140/epjs/s11734-025-01674-0
- 7 S. J. Liu, et al. "Proton-boron fusion scheme taking into account the effects of target degeneracy" *Phys. Rev. Research* 6, 013323 – Published 25 March 2024 DOI: 10.1103/PhysRevResearch.6.013323
- 8 Xiaochuan Ning, et al. "Laser-Driven Proton-Boron Fusions: Influences of the Boron State" *Laser and Particle Beams*, Volume 2022, 2022, e8, DOI: <https://doi.org/10.1155/2022/9868807>
- 9 Daniele Margarone, Julien Bonvalet, Lorenzo Giuffrida, Alessio Morace, Vasiliki Kantarelou, Marco Tosca, Didier Raffestin, Philippe Nicolai, Antonino Picciotto, Yuki Abe, Yasunobu Arikawa, Shinsuke Fujioka, Yuji Fukuda, Yasuhiro Kuramitsu, Hideaki Habara, Dimitri Batani "In-Target Proton-Boron Nuclear Fusion using a PW-class laser" *Applied Sciences*, 2022, 12, 1444. <https://doi.org/10.3390/app12031444>
- 10 Daniele Margarone, Alessio Morace, Julien Bonvalet, Yuki Abe, Vasiliki Kantarelou, Didier Raffestin, Lorenzo Giuffrida, Philippe Nicolai, Marco Tosca, Antonino Picciotto, Giada Petringa, Giuseppe A. P. Cirrone, Yuji Fukuda, Yasuhiro Kuramitsu, Hideaki Habara, Yasunobu Arikawa, Shinsuke Fujioka, Emmanuel D'Humieres, Georg Korn and Dimitri Batani "Generation of α -Particle Beams With a Multi-kJ, Peta-Watt Class Laser System" *Frontiers in Physics* 1 September 2020 | Volume 8 | Article 343, doi: 10.3389/fphy.2020.00343
- 11 Nagai K., Nakajima M., Norimatsu T.Y., Izawa T. and Yamanaka T. "Solvent removal during curing process of highly spheric and monodispersed-sized polystyrene capsules from density-matched emulsions composed of water and benzene/1,2-dichloroethane" *J. Polym. Sci. A* 38 3412 (2000)
- 12 Uchida Y., Takanishi Y. and Yamamoto J. "Controlled fabrication and photonic structure of cholesteric liquid crystalline shells" *Adv. Mater.* 25 3234 (2013)
- 13 Iwasa Y.K., Yamanoi Y., Kaneyasu T. and Norimatsu T. "Controlled generation of double emulsions for laser fusion target fabrication using a glass capillary microfluidic device" *Fusion Sci. Technol.* 73 258 (2018)
- 14 Iwasa Y. et al. "Cu-oleate microspheres fabricated by emulsion method as novel targets for fast ignition laser fusion experiments" *Fusion Eng. Des.* 125 89 (2017)
- 15 T. Xing, S. Mateti, L. Li, F. Ma, A. Du, Y. Gogotsi, Y. Chen, *Sci. Rep.*, 6, 35532 (2016).
- 16 S. Mateti, K. Yang, X. Liu, S. Huang, J. Wang, L. Li, P. Hodgson, M. Zhou, J. He, Y. Chen, *Adv. Func. Mater.*, 28, 1707556 (2018)
- 17 S. Mateti, C. S. Wong, Z. Liu, W. Yang, Y. Li, L. Li, Y. Chen, *Nano Res.*, 11, 334 (2018).
- 18 H. Jiang, Q. Cai, S. Mateti, Y. Yu, C. Zhi, Y. Chen, *ACS, Appl. Mater. Interfaces*, 13, 44751 (2021).
- 19 J Kawanaka, N Miyanaga, H Azechi, T Kanabe, T Jitsuno, K Kondo, Y Fujimoto, N Morio, S Matsuo, Y Kawakami, et al. "3.1-kJ chirped-pulse power amplification in the LFEX laser" *J. Phys.: Conf. Ser.* 112 032006 (2008) DOI 10.1088/1742-6596/112/3/032006
- 20 Lorenzo Giuffrida, Fabio Belloni, Daniele Margarone, Giada Petringa, Giuliana Milluzzo, Valentina Scuderi, Andriy Velyhan, Marcin Rosinski, Antonino Picciotto, et al. "High-current stream of energetic α particles from laser-driven proton-boron fusion" *Phys. Rev. E* 101, 013204 (2020) DOI: <https://doi.org/10.1103/PhysRevE.101.013204>
- 21 Wilks, S. C., Langdon, A. B., Cowan, T. E., Roth, M., Singh, M., Hatchett, S., ... & Snavely, R. A. "Energetic proton generation in ultra-intense laser–solid interactions" *Physics of plasmas*, 8(2), 542-549 (2001)
- 22 C. Perego, D. Batani, A. Zani, and M. Passoni "Target normal sheath acceleration analytical modeling, comparative study and developments" *REVIEW OF SCIENTIFIC INSTRUMENTS* 83, 02B502 (2012)
- 23 M. Passoni, C. Perego, A. Sgattoni, D. Batani "Advances in Target Normal Sheath Acceleration theory" *PHYSICS OF PLASMAS* 20, 060701 (2013)
- 24 D. Batani, G. Boutoux, F. Burgy, K. Jakubowska, and J. E. Ducret "Proton acceleration measurements using fs laser irradiation of foils in the target normal sheath acceleration regime" *Phys. Plasmas*, *Physics of Plasmas* 25, 054506 (2018)
- 25 Vasiliki Kantarelou, Andriy Velyhan, Przemysław Tchórz, Marcin Rosiński, Giada Petringa, Giuseppe Antonio Pablo Cirrone, Valeriia Istoksaia, et al. "A Methodology for the Discrimination of Alpha Particles from other Ions in Laser-Driven Proton-Boron Reactions Using CR-39 Detectors Coupled in a Thomson Parabola Spectrometer" *Laser and Particle Beams*, Volume 2023, e10 (2023) DOI: <https://doi.org/10.1155/2023/3125787>
- 26 J.F. Ziegler, Ziegler M.D., Biersack J.P. "SRIM - The stopping and range of ions in matter" *Nucl. Instruments Methods Phys. Res. Sect. B Beam Interact. with Mater. Atoms*– Vol. 268. – No. 11–12. – P. 1818–1823 (–2010)
- 27 V. Lelasseux, Fuchs J. "Modelling energy deposition in TR image plate detectors for various ion types" *J. Instrum.* Vol. 15. – No. 04. – P. P04002–P04002 (2020)

-
- ²⁸ N. Rabhi, D. Batani, G. Boutoux, J.-E. Ducret, K. Jakubowska, I. Lantuejoul-Thfoin, C. Nauraye, A. Patriarca, A. Saïd, A. Semsoum, L. Serani, B. Thomas, and B. Vauzour «Calibration of imaging plate detectors to mono-energetic protons in the range 1-200 MeV» *Review of Scientific Instruments* 88, 113301 (2017)
- ²⁹ A. Alejo et al., [10.1063/1.4893780](https://doi.org/10.1063/1.4893780)
- ³⁰ M. S. Schollmeier, J. J. Bekx, et al. “Differentiating multi-MeV, multi-ion spectra with CR-39 solid-state nuclear track detectors” *Scientific Reports* volume 13, Article number: 18155 (2023)
- ³¹ J. Derouillat, A. Beck, F. Pérez, T. Vinci, M. Chiaramello, A. Grassi, M. Fle, G. Bouchard, I. Plotnikov, N. Aunai, J. Dargent, C. Riconda, and M. Grech, *Comput. Phys. Commun.* 222, 351 (2018).
- ³² E. Lefebvre et al., “Development and validation of the TROLL radiation-hydrodynamics code for 3D hohlraum calculations,” *Nucl. Fusion* 59, 032010 (2019).
- ³³ Wilks S, Krueer W, Tabak M and Langdon A B, *Phys. Rev. Lett.* 69 1383 (1992).